

The star-forming complex LMC-N79 as a future rival to 30 Doradus

Bram B. Ochsendorf^{1,*}, Hans Zinnecker^{2,3}, Omnarayani Nayak¹, John Bally⁴, Margaret Meixner^{1,5}, Olivia C. Jones⁵, Remy Indebetouw^{6,7} & Mubdi Rahman¹

¹*Department of Physics and Astronomy, The Johns Hopkins University, 3400 North Charles Street, Baltimore, MD 21218, USA, bochsen1@jhu.edu*

²*Deutsches SOFIA Institut (DSI), University of Stuttgart, Pfaffenwaldring 29, D-70569, Germany*

³*Universidad Autonoma de Chile, Santiago de Chile, Chile*

⁴*Astrophysical and Planetary Sciences Department, University of Colorado, UCB 389 Boulder, Colorado 80309, USA*

⁵*Space Telescope Science Institute, 3700 San Martin Drive, Baltimore, MD 21218, USA*

⁶*Department of Astronomy, University of Virginia, PO 400325, Charlottesville, VA 22904, USA*

⁷*National Radio Astronomy Observatory, 520 Edgemont Rd, Charlottesville, VA 22903, USA*

Within the early Universe, ‘extreme’ star formation may have been the norm rather than the exception^{1,2}. Super Star Clusters (SSCs; $M_{\star} \gtrsim 10^5 M_{\odot}$) are thought to be the modern-day analogs of globular clusters, relics of a cosmic time ($z \gtrsim 2$) when the Universe was filled with vigorously star-forming systems³. The giant HII region 30 Doradus in the Large Magellanic Cloud (LMC) is often regarded as a benchmark for studies of extreme star formation⁴. Here, we report the discovery of a massive embedded star forming complex spanning ~ 500 pc in the unexplored southwest region of the LMC, which manifests itself as a younger, embedded twin of 30 Doradus. Previously known as N79, this region has a star formation efficiency exceeding that of 30 Doradus by a factor of ~ 2 as measured over the past $\lesssim 0.5$ Myr. Moreover, at the heart of N79 lies the most luminous infrared (IR) compact source discovered with large-scale IR surveys of the LMC and Milky Way, possibly a precursor to the central SSC of 30 Doradus, R136. The discovery of a nearby candidate SSC may provide invaluable information to understand how extreme star formation proceeds in the current and high-redshift Universe.

The LMC is the prototypical ‘Barred Magellanic Spiral’, a population of galaxies with an asymmetric, sometimes off-centered stellar bar, a single spiral arm, and often a large star forming complex at one end of the bar⁵. More recently, evidence of *multiple* arm-like features extending from the outer disc of the LMC were obtained with high-resolution HI maps⁶, thought to originate from tidal interactions with both the Galaxy and Small Magellanic Cloud (SMC)⁷ (Fig. 1a). In particular, at heliocentric velocities of $\sim 255 - 270$ km s⁻¹ (Fig. 1b) the LMC resembles a barred spiral galaxy with two prominent, opposing arms extending from the eastern (Arm E) and western (Arm W) part of the HI disk.

Arm E culminates in the ‘south-eastern HI overdensity’ located at the leading edge of the LMC’s motion through the Galactic Halo⁸. At the tip of the south-eastern HI overdensity and Arm E lies 30 Doradus, harboring the largest HII region in the Local Group. Ionized gas traces massive star populations with a median age of ~ 4 Myr⁹. In addition, with the use of sensitive,

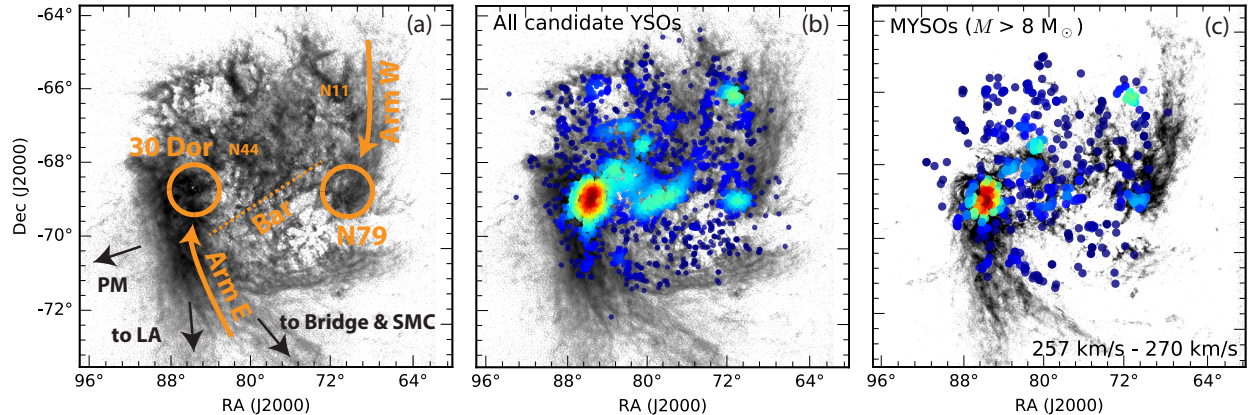


Figure 1: Large-scale structure of the LMC. (a): HI map of the LMC. Black and orange markings highlight locations of prominent features in the LMC and the larger-scale Magellanic complex, such as the asymmetrical, off-centered optical stellar bar (see Fig. 2), and tidal arms E and W. Arm E culminates in the south-eastern HI overdensity, splits at the LMC tidal radius, and subsequently leads to the Magellanic Bridge/SMC and the Leading Arm (LA). The proper motion (PM) of the LMC through the Galaxy is also indicated. In orange we highlight the rotation of the LMC disk³¹ and the locations of several prominent star forming regions. (b): Same as (a), but here we overlay ~ 3500 YSO candidates discovered in various galaxy-wide surveys of the LMC (see Methods). The color code reflects the surface density of YSOs, with red indicating the highest local surface density or intrinsic clustering of these sources. Clearly discerned are the stellar bar and several star forming regions: 30 Doradus, N11, N44, and the relatively unknown complex N79. (c): Same HI map, but only showing the velocity range $257 - 270 \text{ km s}^{-1}$ to accentuate the ‘barred spiral’ appearance of the LMC. Here, we overlay the subset of massive YSOs (MYSOs; $M > 8 M_{\odot}$). Luminous, embedded, and extremely young, these MYSOs offer a snapshot to the massive star formation activity of the LMC averaged over the past $\lesssim 0.5 \text{ Myr}$ ¹⁰.

galaxy-wide IR surveys of the LMC with *Spitzer* and *Herschel*, some ~ 3500 Young Stellar Object (YSO) candidates have been identified through color-magnitude cuts, morphological inspection, and spectroscopic follow-up observations (see Methods). From these YSO candidates, we have identified a subset of *massive* YSOs (MYSOs) that are well characterized by YSO models. This MYSO catalogue is tested to be complete for massive ($M > 8 M_{\odot}$), young ($\lesssim 0.5 \text{ Myr}$) objects, and this data offers a unique snapshot of the *most recent* massive star formation activity of the LMC¹⁰.

In Fig. 1b, we overplot the HI map of the LMC with the location and clustering of YSO candidates found across the galaxy. Several obvious clusterings stand out: the stellar bar (which likely contains many false positives; see Methods), and the well-known star forming regions 30 Doradus, N11 and N44. In addition, Fig. 1b reveals a star forming complex in the relatively unexplored southwest region of the LMC, which coincides with the N79 H II region¹¹. Figure 1c plots the subsample of MYSOs over the HI gas at a velocity range $257 - 270 \text{ km s}^{-1}$, which highlights the tidal arms of the LMC. Most interestingly, both 30 Doradus and N79 are perched on

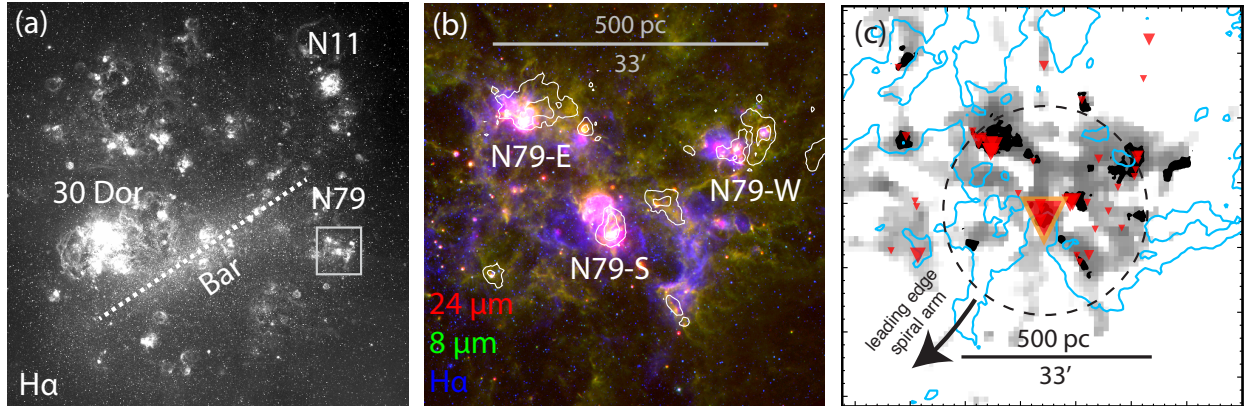


Figure 2: **Dissecting N79.** (a): $H\alpha$ image of the LMC. Highlighted are N79 (grey box), 30 Doradus, N11, and the stellar bar. (b): Blow-up of the N79 region in a three-color image showing $H\alpha$ (blue), Spitzer/IRAC $8\mu\text{m}$ (green), and Spitzer/MIPS $24\mu\text{m}$ (red). White contours show CO clouds from the MAGMA survey, where we identify three main CO sub-complexes: N79-South (S), N79-East (E), and N79-West (W) (c): The CO-based (filled black contour) and dust-based (grayscale) molecular mass in N79, overplotted with the location of MYSOs (inverted red triangles; size reflects source luminosity). Also plotted is the HI gas (blue contours). While CO peaks in distinct regions, harboring apparent clusterings of MYSOs, the entire complex is bridged through molecular gas as traced by dust, which is sensitive to the extended, more diffuse envelopes of GMCs³².

the leading edges or ‘tips’ of the opposite tidal arms E and W, respectively.

The N79 H II region pales in comparison to optically bright star forming regions such as N11 or 30 Doradus (Fig. 2a). Hence, N79 has not been the subject of any prior high-resolution study. However, our IR observations trace the younger, more embedded phase of massive star formation and unveil that the N79 region is a highly efficient star forming engine, exceeding the star formation efficiency of 30 Doradus and N11 by a factor of $\sim 2.0 - 2.5$ (see below).

Spitzer and *Herschel* dissect the structure of the complex, spanning roughly 500 pc, and harboring three main CO complexes: N79-South, N79-East, and N79-West (Fig. 2b). The ^{12}CO (1-0) tracer is known to probe a limited range in volume densities of molecular gas because of critical density, depletion, opacity, and photo-chemical effects. In addition, at the reduced metallicity of the LMC, a significant part of H_2 may be in a ‘CO-dark’ phase¹². By combining far-infrared dust emission and HI one can circumvent these limitations and estimate the H_2 distribution¹³. The dust-based molecular material (Fig. 2c) shows that the entire N79 region consist of one single molecular structure of ~ 500 pc. This unusual large size may be the result of gas accumulation and compression at the tip of Arm W. Star formation concentrates within the molecular material, with apparent clusterings in the CO-emitting clouds (Fig. 2c).

At the heart of the large-scale N79 complex lies an extremely luminous object (Fig. 3a), which immediately draws parallels to the central cluster of 30 Dor, R136 (Nayak et al., in prep). This source has been catalogued¹⁴ as HSOBMHERICC_J72.971176-69.391112, but will be referred to as ‘H72.97-69.39’. At $L_{\text{IR}} \simeq 2.2 \times 10^6 L_{\odot}$ (Fig. 3b), H72.97-69.39 is more luminous than any

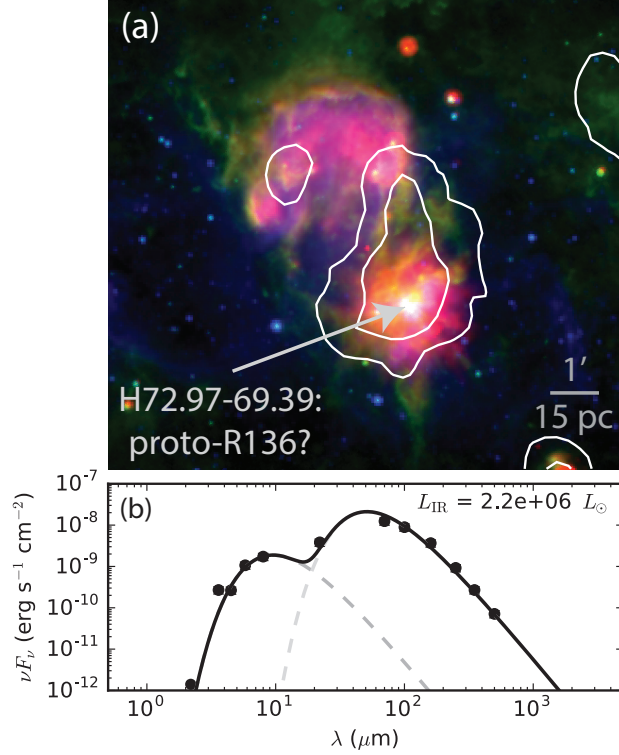


Figure 3: **H72.97-69.39**. (a): The immediate environment of the compact luminous object at the heart of N79, H72.97-69.39, possibly a precursor to the R136 cluster in 30 Doradus (Nayak et al., in prep). (b): Spectral energy distribution of H72.97-69.39 compiled from various ground and space-based surveys (see Methods). A two-temperature modified blackbody yields an infrared luminosity of $L_{\text{IR}} = 2.2 \times 10^6 L_{\odot}$.

MYSO or compact HII region discovered with large-scale IR surveys of the LMC¹⁴ and Milky Way¹⁵. This luminosity is equivalent to more than three O3V stars of $M \sim 70 M_{\odot}$ ¹⁵ or a single very massive star of $\sim 160 M_{\odot}$, using the mass-luminosity relation for upper-main sequence stars¹⁶, $L \propto M^{1.6}$ (at $M \gtrsim 70 M_{\odot}$).

We measure the star formation characteristics of N79 within an aperture of increasing size centered on H72.97-69.39 and compare this with 30 Doradus and N11. The total SFR_{MYSO} is obtained by counting MYSOs and using an initial mass function (IMF) and characteristic age ($t_{\star} \lesssim 0.5$ Myr; see Methods). We then compare SFR_{MYSO} with the SFR measured through $\text{H}\alpha$ and $24 \mu\text{m}$ emission, $\text{SFR}_{\text{H}\alpha}$ (see Methods), which allows us to compare the average SFR over the past ~ 0.5 Myr and ~ 4 Myr, respectively. Figure 4a shows that N79 matches the current SFR_{MYSO} of N11, while being a factor of ~ 2 lower than 30 Doradus. N11 is currently exhibiting a second burst of star formation¹⁷ and shows $\text{SFR}_{\text{MYSO}} \approx \text{SFR}_{\text{H}\alpha}$, thus sustaining its average SFR over the past ~ 4 Myr. 30 Doradus shows $\text{SFR}_{\text{MYSO}} < \text{SFR}_{\text{H}\alpha}$, consistent with its inferred star formation history, which dramatically accelerated roughly ~ 7 Myrs ago, peaked around 1 - 3 Myrs ago, and is currently decelerating¹⁸. Conversely, the SFR in N79 has significantly *increased* over the past few Myr ($\text{SFR}_{\text{MYSO}} > \text{SFR}_{\text{H}\alpha}$) and has yet to reach its peak star formation activity. N79 may

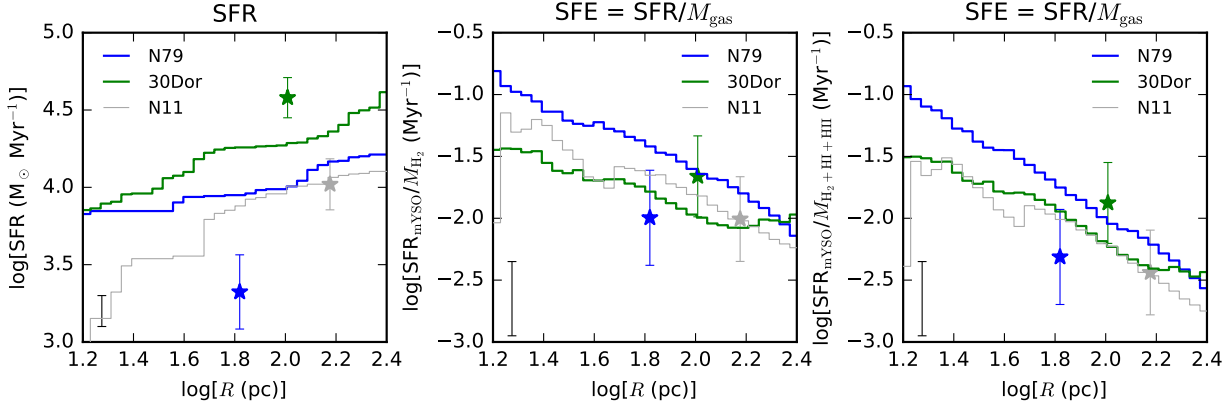


Figure 4: **Star formation properties: N79 versus N11 and 30 Doradus.** (a): The SFR as measured by MYSO counting, SFR_{MYSO} , in apertures of radius R centered on H72.97-69.39 (RA = 72.972, DEC = -69.391), N11 (RA = 74.227, DEC = -66.368), and R136 (RA = 84.633, DEC = -69.092). The asterisks marks the SFR of the regions as measured by $\text{H}\alpha$, $\text{SFR}_{\text{H}\alpha}$, where the size R of the H II regions is defined to enclose 90% of the total flux from the central clusters³³. Error bars are dominated by multiplicity (SFR_{MYSO}) or stochastic sampling of the IMF ($\text{SFR}_{\text{H}\alpha}$; see Methods). (b): The inverse of the gas depletion time, $\text{SFR}/M_{\text{gas}}$, where the gas includes only the molecular component. The error bar shows the absolute uncertainty, dominated by systematic uncertainties in determining the molecular gas mass. However, the relative uncertainties are expected to be lower (see Methods). (c): Same as (b), but now including the molecular, neutral, and ionized components.

therefore be in a similar accelerating star formation phase 30 Doradus was ~ 7 Myrs ago.

By dividing the measured SFR with the total gas reservoir surrounding the star forming complexes, we obtain the inverse of the local gas depletion timescale, $\text{SFR}/M_{\text{gas}}$. This quantity provides a measure of the timescale to exhaust the available gas reservoir at the current SFR (assuming all gas would be converted into stars). While the molecular clouds in the LMC are associated with HI envelopes¹⁹, it is unclear which fraction of M_{HI} will eventually be available for star formation. Therefore, we consider two cases. First, we take $M_{\text{gas}} = M_{\text{H}_2}$, i.e., we only take into account the molecular (dust-based) material (Fig. 4b). Second, we assume $M_{\text{gas}} = M_{\text{H}_2} + M_{\text{HI}} + M_{\text{HII}}$. By combining the molecular (dust-based), neutral, and ionized gas, we attempt to estimate an upper limit to the available gas reservoir for star formation, while tracing gas which may have already been disrupted/dissociated by the ionizing radiation of massive stars. In both cases, it becomes apparent that N79 is the most efficient site of *current* massive star formation, exceeding N11 and 30 Doradus by a factor of $\sim 2.0 - 2.5$.

The total SFR in the LMC from MYSOs is $1.8 \times 10^5 M_{\odot} \text{ Myr}^{-1}$ versus $2.6 \times 10^5 M_{\odot} \text{ Myr}^{-1}$ measured through $\text{H}\alpha$ (see Methods). A percentage of 18%, 9%, and 7% of the total SFR_{MYSO} originates from a ~ 0.25 kpc radius centered on 30 Doradus, N79, and N11, respectively (a 0.25 kpc radius area subtends only 1/400 of the total HI disk⁶). These numbers will likely increase for N79, and decrease for both 30 Doradus and N11 (see above). While the absolute SFR_{MYSO} of

N79 and N11 do not differ significantly at $R \gtrsim 50$ pc (Fig. 4), the star formation efficiency of N79 (through MYSOs) and 30 Doradus (through H α) are elevated compared to N11. This may suggest that the location of 30 Doradus and N79 on the leading edges of Arm E and Arm W positively influences the local star formation efficiency.

Could the central object in N79, H72.97-69.39, eventually evolve into a SSC like R136? The total luminosity of R136, $L_{\text{tot}} \sim 7.0 \times 10^7 L_{\odot}$ ²⁰, is currently at least an order of magnitude higher than H72.97-69.39, $L_{\text{tot}} \sim 2.2 \times 10^6 L_{\odot}$ (Fig. 3b). With a formation period of 5 - 10 Myr¹⁸, an average SFR of $\sim 1 - 2 \times 10^4 M_{\odot} \text{ Myr}^{-1}$ is needed to create a $10^5 M_{\odot}$ stellar cluster, which is a factor of $\sim 1.5 - 3.0$ higher than currently observed at the heart of N79 (Figure 4). However for MYSOs, t_{\star} may be lower than 0.5 Myr¹⁵, which would increase our SFR_{MYSO} estimates through $\text{SFR}_{\text{MYSO}} \propto t_{\star}^{-1}$ (see Methods). The properties of the surrounding gas reservoir also play a role in developing H72.97-69.39. If we assume that the (molecular) gas in N79 is gravitationally collapsing together with a formation timescale of 5 - 10 Myr, a star formation efficiency per free-fall time $\epsilon_{\text{ff}} \sim 0.27 - 0.75$ (0.50 - 0.90 when limiting to the molecular gas) would need to be attained (see Methods). In this regard, values of $\epsilon_{\text{ff}} > 0.50$ have been observed with recent large-scale surveys of individual GMCs in the LMC and Milky Way^{9,21,22,32}, while extraordinary high star formation efficiencies have been quoted for more distant SSCs²³. However, we note that observed values of ϵ_{ff} of individual GMCs extend over several orders of magnitude. Plus, stellar feedback may disrupt the cluster formation process, although the exact effects of feedback on massive protoclusters remain unclear²⁴. Finally, the formation timescale of SSCs may be much smaller than our assumed 5-10 Myr²⁵. All of these effects may limit the final cluster mass. In this regard, detailed follow-up observations with the *Atacama Large Millimeter Array* (ALMA) and the upcoming *James Webb Space Telescope* (JWST) are needed to establish if H72.97-69.39 could evolve into a SSC like R136 ($\sim 10^5 M_{\odot}$), or a less-massive counterpart similar to the Arches and Quintuplet clusters near the Galactic center ($\sim 10^4 M_{\odot}$)²⁶.

The formation of very massive stars and SSCs is poorly understood²⁷. In this regard, our findings on N79 and H72.97-69.39 highlights the importance of high-resolution IR observations to unveil the earliest phases of extreme star formation. The unique location of 30 Doradus and N79 suggest that the crossroads of spiral arms and galactic bars-ends may provide the right physical conditions to create massive clusters²⁸. However, other factors that may play a role are the area-normalized SFR of a galaxy²⁹, accretion flows²³, or tidal interactions⁷: observations suggest that R136 formed after a recent collision of distinct HI flows, which were initially induced by the last LMC - SMC interaction ~ 0.2 Gyr ago³⁰. Because of the proximity and face-on orientation of the LMC, ALMA and JWST will allow to spatially resolve the formation of this candidate SSC down to $\lesssim 0.02$ pc scales, which may reveal in exquisite detail how extreme star formation ignites and proceeds in the current and high-redshift Universe.

1. Barger, A. J. *et al.* Submillimetre-wavelength detection of dusty star-forming galaxies at high redshift. *Nature* **394**, 248–251 (1998). astro-ph/9806317.
2. Turner, J. L. Extreme Star Formation. *Astrophysics and Space Science Proceedings* **10**, 215 (2009). 1009.1416.

3. Kruijssen, J. M. D. Globular clusters as the relics of regular star formation in ‘normal’ high-redshift galaxies. *MNRAS* **454**, 1658–1686 (2015). 1509.02163.
4. Walborn, N. R. The Starburst Region 30 Doradus. In Haynes, R. & Milne, D. (eds.) *The Magellanic Clouds*, vol. 148 of *IAU Symposium*, 145 (1991).
5. de Vaucouleurs, G. & Freeman, K. C. Structure and dynamics of barred spiral galaxies, in particular of the Magellanic type. *Vistas in Astronomy* **14**, 163–294 (1972).
6. Staveley-Smith, L., Kim, S., Calabretta, M. R., Haynes, R. F. & Kesteven, M. J. A new look at the large-scale HI structure of the Large Magellanic Cloud. *MNRAS* **339**, 87–104 (2003). astro-ph/0210501.
7. Bekki, K. & Chiba, M. Dynamical Influences of the Last Magellanic Interaction on the Magellanic Clouds. *PASA* **24**, 21–29 (2007). astro-ph/0603812.
8. de Boer, K. S., Braun, J. M., Vallenari, A. & Mebold, U. Bow-shock induced star formation in the LMC? *A&A* **329**, L49–L52 (1998). astro-ph/9711052.
9. Murray, N. Star Formation Efficiencies and Lifetimes of Giant Molecular Clouds in the Milky Way. *ApJ* **729**, 133 (2011). 1007.3270.
10. Ochsendorf, B. B., Meixner, M., Chastenet, J., Tielens, A. G. G. M. & Roman-Duval, J. The Location, Clustering, and Propagation of Massive Star Formation in Giant Molecular Clouds. *ApJ* **832**, 43 (2016). 1609.03522.
11. Henize, K. G. Catalogues of H α -emission Stars and Nebulae in the Magellanic Clouds. *ApJS* **2**, 315 (1956).
12. Madden, S. C., Poglitsch, A., Geis, N., Stacey, G. J. & Townes, C. H. [C II] 158 Micron Observations of IC 10: Evidence for Hidden Molecular Hydrogen in Irregular Galaxies. *ApJ* **483**, 200–209 (1997).
13. Jameson, K. E. *et al.* The Relationship Between Molecular Gas, H I, and Star Formation in the Low-mass, Low-metallicity Magellanic Clouds. *ApJ* **825**, 12 (2016). 1510.08084.
14. Seale, J. P. *et al.* Herschel Key Program Heritage: a Far-Infrared Source Catalog for the Magellanic Clouds. *AJ* **148**, 124 (2014).
15. Mottram, J. C. *et al.* The RMS Survey: The Luminosity Functions and Timescales of Massive Young Stellar Objects and Compact H II Regions. *ApJ* **730**, L33 (2011). 1102.4702.
16. Zinnecker, H. & Yorke, H. W. Toward Understanding Massive Star Formation. *ARA&A* **45**, 481–563 (2007). 0707.1279.
17. Walborn, N. R. & Parker, J. W. Two-stage starbursts in the Large Magellanic Cloud - N11 as a once and future 30 Doradus. *ApJ* **399**, L87–L89 (1992).

18. Cignoni, M. *et al.* Hubble Tarantula Treasury Project. II. The Star-formation History of the Starburst Region NGC 2070 in 30 Doradus. *ApJ* **811**, 76 (2015). 1505.04799.
19. Fukui, Y. *et al.* Molecular and Atomic Gas in the Large Magellanic Cloud. II. Three-dimensional Correlation Between CO and H I. *ApJ* **705**, 144–155 (2009). 0909.0382.
20. Malumuth, E. M. & Heap, S. R. UBV stellar photometry of the 30 Doradus region of the large Magellanic Cloud with the Hubble Space Telescope. *AJ* **107**, 1054–1066 (1994).
21. Lee, E. J., Miville-Deschênes, M.-A. & Murray, N. W. Observational Evidence of Dynamic Star Formation Rate in Milky Way Giant Molecular Clouds. *ApJ* **833**, 229 (2016). 1608.05415.
22. Vutisalchavakul, N., Evans, N. J., II & Heyer, M. Star Formation Relations in the Milky Way. *ApJ* **831**, 73 (2016). 1607.06518.
23. Turner, J. L. *et al.* Highly efficient star formation in NGC 5253 possibly from stream-fed accretion. *Nature* **519**, 331–333 (2015). 1503.05254.
24. Ginsburg, A. *et al.* Toward gas exhaustion in the W51 high-mass protoclusters. *A&A* **595**, A27 (2016). 1605.09402.
25. Crowther, P. A. *et al.* The R136 star cluster dissected with Hubble Space Telescope/STIS. I. Far-ultraviolet spectroscopic census and the origin of He II λ 1640 in young star clusters. *MNRAS* **458**, 624–659 (2016). 1603.04994.
26. Figer, D. F. *et al.* Hubble Space Telescope/NICMOS Observations of Massive Stellar Clusters near the Galactic Center. *ApJ* **525**, 750–758 (1999). astro-ph/9906299.
27. Krumholz, M. R. The Formation of Very Massive Stars. In Vink, J. S. (ed.) *Very Massive Stars in the Local Universe*, vol. 412 of *Astrophysics and Space Science Library*, 43 (2015). 1403.3417.
28. Athanassoula, E. The existence and shapes of dust lanes in galactic bars. *MNRAS* **259**, 345–364 (1992).
29. Johnson, L. C. *et al.* Panchromatic Hubble Andromeda Treasury. XVIII. The High-mass Truncation of the Star Cluster Mass Function. *ApJ* **839**, 78 (2017). 1703.10312.
30. Fukui, Y. *et al.* Formation of the young massive cluster R136 triggered by tidally-driven colliding H I flows. *PASJ* **69**, L5 (2017). 1703.01075.
31. van der Marel, R. P. & Kallivayalil, N. Third-epoch Magellanic Cloud Proper Motions. II. The Large Magellanic Cloud Rotation Field in Three Dimensions. *ApJ* **781**, 121 (2014). 1305.4641.

32. Ochsendorf, B. B., Meixner, M., Roman-Duval, J., Rahman, M. & Evans, N. J., II. What Sets the Massive Star Formation Rates and Efficiencies of Giant Molecular Clouds? *ApJ* **841**, 109 (2017). 1704.06965.
33. Lopez, L. A. *et al.* The Role of Stellar Feedback in the Dynamics of H II Regions. *ApJ* **795**, 121 (2014). 1309.5421.

Author correspondence. Correspondence and request for materials should be directed to B. B. Ochsendorf.

Author contributions. B. B. O. performed the analysis, coordinated collaboration, and wrote the manuscript. O. N. helped characterizing H72.97-69.39. M. M. and O. C. J. helped with the creation of the MYSO catalog and estimates of source contamination. H. Z., J. B., R. I., and M. R. provided help with the interpretation of the results and implications.

Methods

LMC surveys. In this work we have made use of various galaxy-wide surveys of the LMC:

1. *Atomic gas:* 21 cm data from the Australian Telescope Compact Array and Parkes 64 m radio Telescope map³⁴.
2. *Molecular gas:* ^{12}CO (1-0) data from the Magellanic Mopra Assessment³⁵ (MAGMA) Data Release 2 (resolution 45”).
3. *Ionized gas:* $\text{H}\alpha$ from the Southern H-Alpha Sky Survey Atlas³⁶ (SHASSA) was used for calculating the ionized gas mass. The $\text{H}\alpha$ image displayed in Figure 2a stems from the Magellanic Clouds Emission Line Survey³⁷ (MCELS), which has higher resolution compared to SHASSA but is not calibrated nor continuum subtracted.
4. *Infrared:* 3.6, 4.5, 5.8, and 8.0 μm mid-IR data from Spitzer’s Surveying the Agents of a Galaxy’s Evolution³⁸ (SAGE) and 70, 160, 250, 350, and 500 μm far-IR data from the Herschel Inventory of the Agents of Galaxy Evolution³⁹ (HERITAGE).

MYSO selection & completeness. We have compiled a catalog of (highly) probable YSOs by combining the results of galaxy-wide searches of YSO candidates^{14,40–42} using SAGE and HERITAGE data. The creation of the catalogue is explained in detail elsewhere¹⁰, but the essential points are discussed here as well.

YSO candidates are identified through careful selection criteria (e.g., color-magnitude cuts, morphological inspection) tailored to minimize contamination from sources such as planetary nebulae, evolved stars, and background galaxies. Contamination estimates range from $\sim 55\%$ ⁴⁰ to $\sim 10\%$ ¹⁴. This means that in regions of high source density (such as the stellar bar), a relatively large amount of false source candidates can be expected (see Figure 1b). However, contamination levels vary between the faint and bright end of the YSO distribution, as faint YSOs overlap more with the aforementioned contaminants in color-magnitude space compared to their luminous (i.e., higher-mass) counterparts. For high mass YSO candidates, the contamination from evolved stars and background galaxies is shown to be $\lesssim 20\%$ ⁴³. However, in star-forming regions the contamination becomes negligible ($< 1\%$) once SED fitting criteria has been applied.

We combine the high-probable YSO candidates from the aforementioned studies^{14,40,41} and subsequently fit their spectral energy distributions with YSO models⁴⁴. These models (2×10^5 in total) cover a wide range of physical parameters for different stages in the YSO evolutionary path, often divided in Stage 1 (least evolved), 2, and 3 (most evolved). The stringent color cuts used to separate out YSOs from fore- and background contaminations renders our census of Stage 2 and Stage 3 sources incomplete. However, these sources are largely irrelevant to this work since we aim to probe youngest population of YSOs, i.e., the earliest stages of (massive) star formation.

The age of Stage 1 MYSOs is estimated at 0.5 Myr, which is the most recent value obtained for the observationally-derived ‘Class 1’ low-mass sources (which largely overlap with the theoretically-based ‘Stage 1’ sources^{45,46}) in the Gould’s Belt⁴⁷. It is not clear whether this value applies to massive stars; the absolute durations of the starless and active star-forming phases for

massive protostars is highly uncertain⁴⁸. In addition, the accreting phase for massive protostars may decrease with luminosity, possibly reaching 0.1 Myr for a $10^5 L_{\odot}$ star¹⁵. Indeed, massive stars are expected to evolve more quickly than their lower-mass counterparts, and the assumed age may therefore represent an upper limit to the age of these systems. A younger age would impact our results by *increasing* our SFR through $\text{SFR} \propto t_{\star}^{-1}$, where t_{\star} is the age of the YSO population.

Completeness of the YSO catalogues has been evaluated through false source extraction tests for both the SAGE⁴¹ and HERITAGE³⁹ data, and conclude that our catalogue of YSOs should be complete for Stage 1 MYSOs of $M > 8 M_{\odot}$ ($L \gtrsim 10^3 L_{\odot}$). We set the photometric errors to 10% in the 2MASS, IRAC, and MIPS bands, which allows to account for multiple sources of error (systematic, calibration, variability, photon-counting)⁴⁰. However, as PAH emission is not incorporated into the SED models (which will alter the emission in the 3.6, 5.8, and 8.0 μm bands compared to the models), we relax our constraints and adjust the error bars in these bands to 20%, 30%, and 40%, respectively, corresponding to the intrinsic strengths of the PAH bands⁴⁹. For the HERITAGE data, other sources of uncertainty were considered as well (background, PSF shapes)³⁹: typical uncertainties reported in the HERITAGE catalog are of order 5% - 20%. We only consider ‘well-fitted’ sources, i.e. those yielding reduced chi square of $\chi_{\text{red}}^2 \leq 5$ with the YSO models. By choosing to remove sources above a fixed reduced chi-squared value further decreases our source contamination. However, poorly-fitted sources may also arise because of a bad data point, a mismatch in photometric bands because of variability, multiplicity, or inadequacies of the YSO models⁴⁰. Therefore, we stress that a poor fit does not necessarily mean that the object is not a YSO. We ultimately end with a catalogue of 693 Stage 1 MYSOs ($M > 8 M_{\odot}$) across the LMC.

Spectral energy distribution of H72.97-69.39. The spectral energy distribution of the central luminous source H72.97-69.39 was compiled from the InfraRed Survey Facility (IRSF)⁵⁰, WISE⁵¹, SAGE³⁸, and HERITAGE³⁹. Its exceptional brightness and extended morphology causes the YSO model to severely underestimate its far-IR flux⁵². Instead, we use a simple two-temperature modified blackbody (MBB) function, where the temperature T , spectral index β , and scaling parameters are left as free parameters⁵³. The temperature of the hot dust component, peaking at $\sim 10 \mu\text{m}$, radiates at $T_1 = 300 \text{ K}$ (with $\beta_1 = 0.8$), while the cold component peaking at $\sim 50 \mu\text{m}$ has $T_2 = 60 \text{ K}$ (with $\beta_2 = 0.8$). From this, we obtain a total infrared luminosity of $L_{\text{IR}} = 2.2 \times 10^6 M_{\text{sun}}$.

Mass determination. The mass in N79, N11, and 30 Doradus in the various phases of the ISM (Fig. 4) is estimated in the following ways:

1. *Neutral atomic mass:* assuming the HI gas is optically thin, the column density is estimated through $N_{\text{HI}} = X_{\text{HI}} W_{\text{HI}}$, where W_{HI} is the integrated HI intensity and $X_{\text{HI}} = 1.82 \times 10^{18} \text{ H cm}^2/(\text{K km s}^{-1})$ is the proportionality constant⁵⁴. This can subsequently be converted to gas surface density in $M_{\odot} \text{ pc}^{-2}$ with $\Sigma_{\text{HI}} = 0.8 \times 10^{-20} N_{\text{HI}}$. We note that optically thick and/or cold HI gas emits disproportionately compared to optically thin HI. From absorption spectra it is known that the 21 cm line may be optically thick in the LMC⁵⁵. Many studies have attempted to estimate the optical depth correction to the HI mass, with differences of 10% to 30% reported compared to optically thin gas^{56,57}. Thus, we adopt an uncertainty of 0.1 dex for the HI mass.

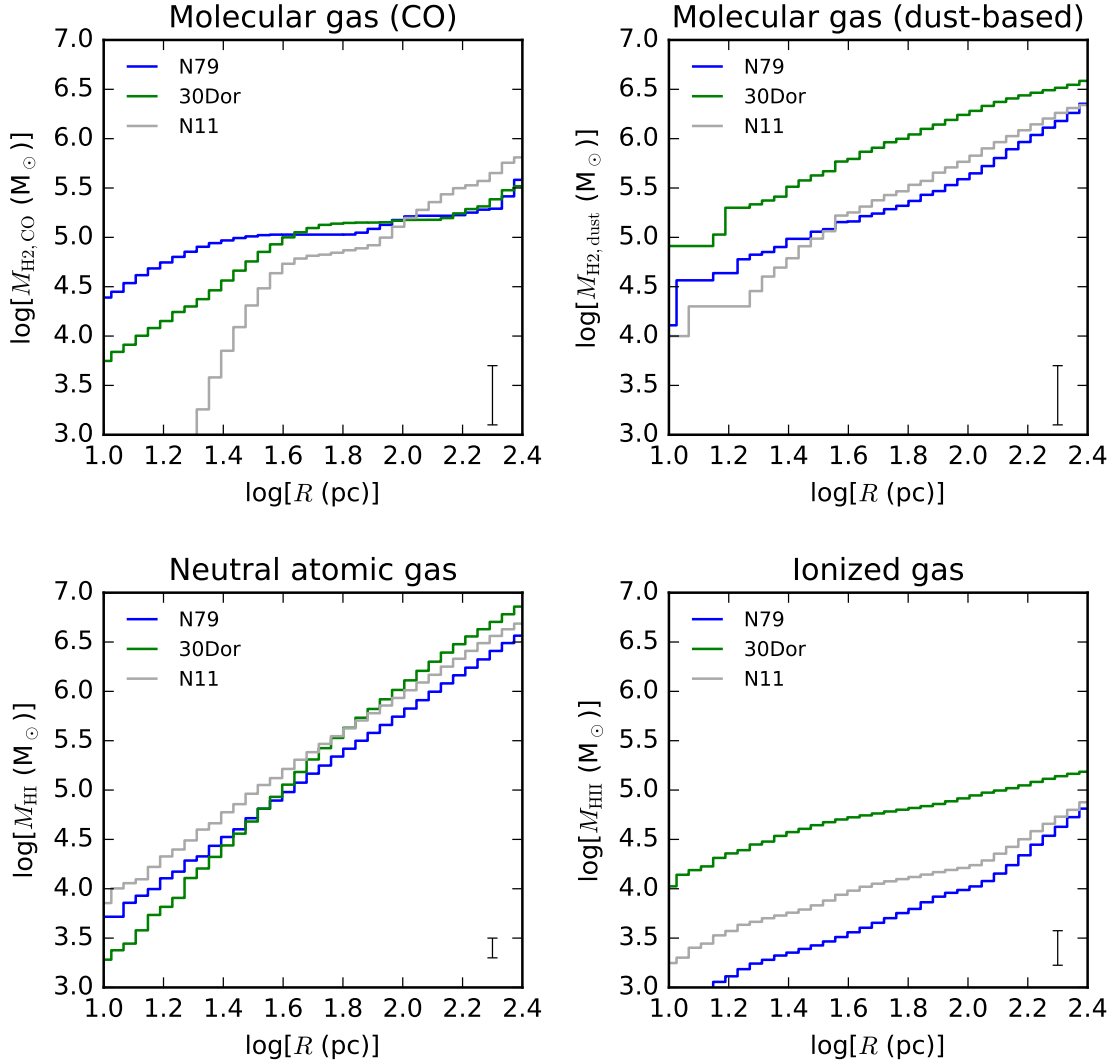


Figure 5: **ISM properties of N79, N11, and 30 Doradus.** The molecular (CO-based and dust-based), neutral, and ionized gas in apertures of radius R centered on N79 (RA = 72.972, DEC = -69.391), 30 Doradus (RA = 84.633, DEC = -69.092), and N11 (RA = 74.227, DEC = -66.368).

2. *CO-based molecular mass*: estimated through $M = \alpha_{\text{CO}} L_{\text{CO}}$, where L_{CO} is the CO luminosity and $\alpha_{\text{CO}} = 8.6 \text{ (K km s}^{-1} \text{ pc}^2)^{-1}$ is the proportionality constant appropriate for the LMC⁵⁸. The α_{CO} factor is expected to be accurate within $\sim 0.3 \text{ dex}^{58}$.
3. *Dust-based molecular mass*: obtained by subtracting from the gas surface density, based on far-infrared dust emission (modeled with a single temperature blackbody modified by a broken power-law emissivity⁵³), the surface density of atomic hydrogen. The creation of this map is discussed in detail elsewhere¹³, but the main caveats are reiterated here. First, the optical thin limit was used to convert HI intensity to column density (see above). Second, it

was assumed that the gas-to-dust ratio in the diffuse and atomic gas is the same as in molecular regions. However, there is mounting evidence that this gas-to-dust ratio changes between different phases of the ISM, with lower gas-to-dust ratios in the dense phase compared to the diffuse phase⁵⁹. Both optically thick HI and a decrease in the gas-to-dust ratio may lead to an overestimation of the dust-based molecular gas. These effects introduce a systematic uncertainty of ~ 0.3 dex in the dust-based molecular gas estimate¹³. However, given that we are focussing on (dense) star forming regions only, these uncertainties will propagate similarly for 30 Doradus, N11, and N79, and therefore the relative uncertainties are expected to be smaller.

4. *Ionized gas*: HII column density in cm^{-2} can be obtained by estimating electron densities in different brightness regimes⁶⁰, which can then be converted to gas surface density in $M_{\odot} \text{pc}^{-2}$ through $\Sigma_{\text{HII}} = 0.8 \times 10^{-20} N_{\text{HII}}$. The systematic uncertainty is estimated at ~ 0.2 dex. This mainly stems from the conversion from $\text{H}\alpha$ intensity to emission measure, which depends on the assumed electron temperature, which can vary⁶¹ within a factor of ~ 2 , leading to a $\sim 50\%$ difference (~ 0.2 dex) in conversion from $\text{H}\alpha$ intensity to emission measure⁶².

Figure 5 shows the molecular (CO and dust-based), neutral, and ionized gas mass. Note that the total CO-based molecular mass in 30 Doradus and N79 are very similar within 100 pc. However, the dust-based molecular mass in 30 Doradus exceeds the CO-based material by almost an order of magnitude, indicating that the bulk of molecular material around 30 Doradus resides in the ‘CO-dark’ phase, possibly through the local intense radiation field from R136. The ionized gas content around the clusters both reflect the mass (i.e., ionizing photon budget) of the central cluster and the evolutionary state (i.e., embeddedness) of the region.

Virial analysis. The virial parameter, $\alpha_{\text{vir}} = 5\sigma_{\text{v}}^2 R / (GM)$ ⁶³, where σ_{v}^2 is the luminosity-weighted (one-dimensional) CO velocity dispersion, G is the gravitational constant, and M the CO mass, can be used to determine whether a cloud (complex) is bound and can undergo collapse, or is unbound, and may expand and dissolve back into the ISM. The critical virial parameter is $\alpha_{\text{cr}} \simeq 2$, with bound clouds having $\alpha_{\text{cr}} \leq 2$. However, lower values for α_{cr} are possible in the case of strong magnetic fields⁶⁴.

Figure 6 shows that the molecular gas in the entire N11 region contains extreme high α_{vir} , which is to be expected given the evolved state of the region, with an expanding ring of material moving outward from the central ‘hole’, where an earlier generation of massive stars appear to have been born⁶⁵ (note that individual cloud fragments may still be collapsing). 30 Doradus also contains elevated α_{vir} ; higher-resolution studies show that the CO gas in 30 Doradus has elevated CO linewidths, probably due to the highly energetic environmental conditions within 30 Doradus⁶⁶. Conversely, N79 reveals sub-critical α_{vir} throughout the majority part of the N79 cloud complex. This indicates that the N79 cloud complex is bound, and may be in a collapsing state.

Star formation rates (SFR) from MYSOs. Young Stellar Objects (YSOs) can be used to obtain a direct measure of SFR through $\text{SFR} = N(\text{YSOs}) \times \langle M_{\star} \rangle / t_{\star}$. Here, $\langle M_{\star} \rangle \approx 0.5$ is the average

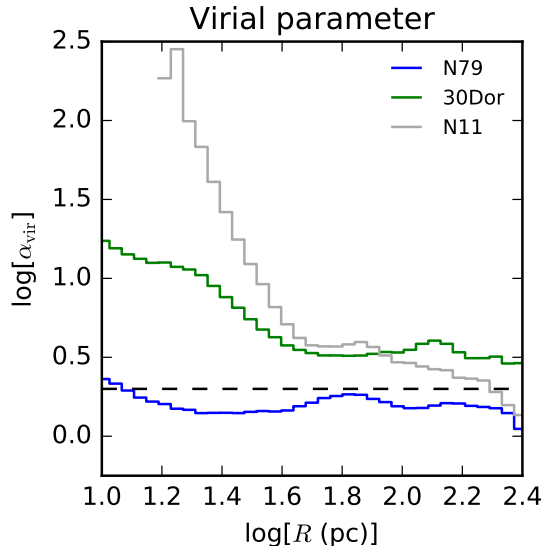


Figure 6: **Virial analysis.** The virial parameter α_{vir} plotted versus radius R in N79, N11, and 30 Doradus.

mass for a fully-sampled IMF⁶⁷. Whereas counting YSOs has previously been applied in studies of nearby molecular clouds, in the LMC we are limited to bright objects. Here, we assume that the luminosity of an MYSO is dominated by a single source. This assumption is motivated by observations of nearby star clusters (e.g., the Orion Trapezium¹⁰). Subsequently, we use YSO models to estimate the mass of each individual source⁴⁴ and multiply the source mass with an IMF⁶⁷ to account for completeness. We choose 0.5 Myr for t_* (but see above). With these assumptions, the completeness limit ($M > 8 M_{\odot}$) translates to a lower limit of $\text{SFR}_{\text{MYSO}} \sim 100 M_{\odot} \text{ Myr}^{-1}$ which we can detect in our observations of the LMC.

Many of the sources in our MYSO sample will break into small clusters when observed at high resolution^{68,69}. We estimate the uncertainty in our SFR_{MYSO} measurement associated with multiplicity as follows. The reprocessed IR luminosity of the Orion Trapezium cluster would appear as a compact source at the resolution of our LMC IR maps. In the Orion Trapezium, the main ionizing source θ^1 Ori C emits $\simeq 50\%$ of the total luminosity of the cluster⁷⁰⁻⁷². The IR luminosity would thus overestimate the luminosity of a single most massive source by a factor of ~ 0.3 dex, which translates to an error of ~ 0.1 dex in mass¹⁵. Therefore, we adopt 0.1 dex as our systematic uncertainty in SFR_{MYSO} ; note that this assumes that the evolutionary tracks used in the YSO models are correct⁷³.

Star formation rates (SFR) from $\text{H}\alpha + 24 \mu\text{m}$. We convolve the $24 \mu\text{m}$ map (from SAGE³⁹) to the resolution of our $\text{H}\alpha$ map (resolution $0.8''$; from SHASSA⁷⁴), and correct the $\text{H}\alpha$ emission for extinction using the $24 \mu\text{m}$ emission. We then transform the combined $\text{H}\alpha$ and $24 \mu\text{m}$ luminosity,

$L(\text{H}\alpha)$ and $L(24\mu\text{m})$, to a SFR⁷⁵ :

$$\text{SFR}_{\text{H}\alpha} (M_{\odot} \text{ yr}^{-1}) = 5.3 \times 10^{-42} [L(\text{H}\alpha) + 0.031 L(24\mu\text{m})]. \quad (1)$$

We note that Eq. 1 assumes a fully-sampled IMF, which can be attained by averaging over large spatial scales⁷⁶ such that each phase of star formation is probed. When studying star formation on smaller scales⁷⁷ these assumption may break down, which introduces stochastic effects that mainly affect the high-end part of the IMF. To account for this, we use the tool ‘Stochastically Lighting Up Galaxies’ (SLUG⁷⁶) to estimate to which extend stochastic sampling of the IMF affect our measured SFR. This process is fully described elsewhere³². The total SFR in the LMC measured through H α equals⁷⁸ $2.6 \times 10^5 M_{\odot} \text{ Myr}^{-1}$.

Star formation efficiency per free-fall time. Can H72.97-69.39 become a $10^5 M_{\odot}$ star cluster? The current state of the (molecular) gas in N79 reveals that it is gravitationally bound and prone to further collapse (Figure 6). We thus assume that the gas collapses on its gravitational timescale, the free-fall time $\tau_{\text{ff}} = \sqrt{3\pi/32G\rho}$, where $\rho = M_{\text{cloud}}/(4/3\pi R_{\text{cloud}}^3)$ is the mean density, M_{cloud} the cloud mass, R_{cloud} the cloud radius, and G the gravitational constant. We adopt a formation timescale of 5 - 10 Myr, motivated by the star formation history of the NGC2070 region¹⁸ (including R136). In this timescale, we calculate that a total of $1.3 - 3.7 \times 10^5$ of mass (molecular and atomic) can collapse to the centre of the N79 cloud from $R_{\text{cloud}} \lesssim 30 - 60$ pc. Thus, to create a $10^5 M_{\odot}$ stellar cluster, a star formation efficiency per free-fall time (i.e., the fraction of mass that is transformed into stars⁷⁹ during τ_{ff}) of $\epsilon_{\text{ff}} \sim 0.27 - 0.75$ (0.50 - 0.90 when only considering molecular gas) would be required.

The question whether or not a $10^5 M_{\odot}$ cluster is massive enough to eventually become a globular cluster ($\gtrsim 10^5 M_{\odot}$)⁸⁰ is not clear, given that young stellar clusters may lose a significant amount of mass through supernovae, stellar winds, and stripping⁸¹⁻⁸³.

Data availability statement. The data and analysis scripts that support the plots within this paper and other findings of this study will be made available through a public repository: www.github.com/bramochsendorf. Additional requests can be directed to the corresponding author.

34. Kim, S. *et al.* A Neutral Hydrogen Survey of the Large Magellanic Cloud: Aperture Synthesis and Multibeam Data Combined. *ApJS* **148**, 473–486 (2003).
35. Wong, T. *et al.* The Magellanic Mopra Assessment (MAGMA). I. The Molecular Cloud Population of the Large Magellanic Cloud. *ApJS* **197**, 16 (2011). 1108.5715.
36. Gaustad, J. E., McCullough, P. R., Rosing, W. & Van Buren, D. A Robotic Wide-Angle H α Survey of the Southern Sky. *PASP* **113**, 1326–1348 (2001). [astro-ph/0108518](https://arxiv.org/abs/astro-ph/0108518).
37. Smith, R. C. & MCELS Team. The UM/CTIO Magellanic Cloud emission-line survey. *PASA* **15**, 163–64 (1998).

38. Meixner, M. *et al.* Spitzer Survey of the Large Magellanic Cloud: Surveying the Agents of a Galaxy's Evolution (SAGE). I. Overview and Initial Results. *AJ* **132**, 2268–2288 (2006). [astro-ph/0606356](#).
39. Meixner, M. *et al.* The HERSCHEL Inventory of The Agents of Galaxy Evolution in the Magellanic Clouds, a Herschel Open Time Key Program. *AJ* **146**, 62 (2013).
40. Whitney, B. A. *et al.* Spitzer Sage Survey of the Large Magellanic Cloud. III. Star Formation and ~1000 New Candidate Young Stellar Objects. *AJ* **136**, 18–43 (2008).
41. Gruendl, R. A. & Chu, Y.-H. High- and Intermediate-Mass Young Stellar Objects in the Large Magellanic Cloud. *ApJS* **184**, 172–197 (2009). [0908.0347](#).
42. Seale, J. P. *et al.* The Evolution Of Massive Young Stellar Objects in the Large Magellanic Cloud. I. Identification and Spectral Classification. *ApJ* **699**, 150–167 (2009). [0904.1825](#).
43. Jones, O. C. *et al.* The SAGE-Spec Spitzer Legacy program: The life-cycle of dust and gas in the Large Magellanic Cloud. Point source classification III. *ArXiv e-prints* (2017). [1705.02709](#).
44. Robitaille, T. P., Whitney, B. A., Indebetouw, R., Wood, K. & Denzmore, P. Interpreting Spectral Energy Distributions from Young Stellar Objects. I. A Grid of 200,000 YSO Model SEDs. *ApJS* **167**, 256–285 (2006). [astro-ph/0608234](#).
45. Heiderman, A. & Evans, N. J., II. The Gould Belt 'MISFITS' Survey: The Real Solar Neighborhood Protostars. *ApJ* **806**, 231 (2015). [1503.06810](#).
46. Heyer, M. *et al.* The rate and latency of star formation in dense, massive clumps in the Milky Way. *A&A* **588**, A29 (2016). [1601.06875](#).
47. Dunham, M. M. *et al.* Young Stellar Objects in the Gould Belt. *ApJS* **220**, 11 (2015). [1508.03199](#).
48. Battersby, C., Bally, J. & Svoboda, B. The Lifetimes of Phases in High-mass Star-forming Regions. *ApJ* **835**, 263 (2017). [1702.02199](#).
49. Carlson, L. R. *et al.* A Panchromatic View of NGC 602: Time-resolved Star Formation with the Hubble and Spitzer Space Telescopes. *ApJ* **730**, 78 (2011). [1012.3406](#).
50. Kato, D. *et al.* The IRSF Magellanic Clouds Point Source Catalog. *PASJ* **59**, 615–641 (2007).
51. Wright, E. L. *et al.* The Wide-field Infrared Survey Explorer (WISE): Mission Description and Initial On-orbit Performance. *AJ* **140**, 1868–1881 (2010). [1008.0031](#).
52. Sewiło, M. *et al.* The youngest massive protostars in the Large Magellanic Cloud. *A&A* **518**, L73 (2010). [1005.2592](#).

53. Gordon, K. D. *et al.* Dust and Gas in the Magellanic Clouds from the HERITAGE Herschel Key Project. I. Dust Properties and Insights into the Origin of the Submillimeter Excess Emission. *ApJ* **797**, 85 (2014). 1406.6066.
54. Spitzer, L. *Physical processes in the interstellar medium* (1978).
55. Marx-Zimmer, M. *et al.* A study of the cool gas in the Large Magellanic Cloud. I. Properties of the cool atomic phase - a third H I absorption survey. *A&A* **354**, 787–801 (2000).
56. Dickey, J. M., Mebold, U., Stanimirovic, S. & Staveley-Smith, L. Cold Atomic Gas in the Small Magellanic Cloud. *ApJ* **536**, 756–772 (2000).
57. Lee, M.-Y., Stanimirović, S., Murray, C. E., Heiles, C. & Miller, J. Cold and Warm Atomic Gas around the Perseus Molecular Cloud. II. The Impact of High Optical Depth on the HI Column Density Distribution and Its Implication for the HI-to-H₂ Transition. *ApJ* **809**, 56 (2015). 1504.07405.
58. Bolatto, A. D., Wolfire, M. & Leroy, A. K. The CO-to-H₂ Conversion Factor. *ARA&A* **51**, 207–268 (2013). 1301.3498.
59. Roman-Duval, J. *et al.* Dust and Gas in the Magellanic Clouds from the HERITAGE Herschel Key Project. II. Gas-to-dust Ratio Variations across Interstellar Medium Phases. *ApJ* **797**, 86 (2014). 1411.4552.
60. Paradis, D. *et al.* Spitzer Characterization of Dust in the Ionized Medium of the Large Magellanic Cloud. *ApJ* **735**, 6 (2011). 1104.1098.
61. Shaver, P. A., McGee, R. X., Newton, L. M., Danks, A. C. & Pottasch, S. R. The galactic abundance gradient. *MNRAS* **204**, 53–112 (1983).
62. Dickinson, C., Davies, R. D. & Davis, R. J. Towards a free-free template for CMB foregrounds. *MNRAS* **341**, 369–384 (2003). astro-ph/0302024.
63. Bertoldi, F. & McKee, C. F. Pressure-confined clumps in magnetized molecular clouds. *ApJ* **395**, 140–157 (1992).
64. Kauffmann, J., Pillai, T. & Goldsmith, P. F. Low Virial Parameters in Molecular Clouds: Implications for High-mass Star Formation and Magnetic Fields. *ApJ* **779**, 185 (2013). 1308.5679.
65. Rosado, M. *et al.* Formation of the nebular complex N11 in the Large Magellanic Cloud. *A&A* **308**, 588–600 (1996).
66. Nayak, O. *et al.* Studying Relation Between Star Formation and Molecular Clumps on Sub-parsec Scales in 30 Doradus. *ArXiv e-prints* (2016). 1608.05451.
67. Kroupa, P. On the variation of the initial mass function. *MNRAS* **322**, 231–246 (2001). astro-ph/0009005.

68. Vaidya, K., Chu, Y.-H., Gruendl, R. A., Chen, C.-H. R. & Looney, L. W. A Hubble Space Telescope View of the Interstellar Environments of Young Stellar Objects in the Large Magellanic Cloud. *ApJ* **707**, 1417–1426 (2009). 0910.5901.
69. Stephens, I. W. *et al.* Stellar Clusterings around "Isolated" Massive YSOs in the LMC. *ApJ* **834**, 94 (2017). 1609.04399.
70. Vacca, W. D., Garmany, C. D. & Shull, J. M. The Lyman-Continuum Fluxes and Stellar Parameters of O and Early B-Type Stars. *ApJ* **460**, 914 (1996).
71. O'dell, C. R., Valk, J. H., Wen, Z. & Meyer, D. M. Identification of velocity systems in the inner Orion nebula. *ApJ* **403**, 678–683 (1993).
72. Simón-Díaz, S., Herrero, A. & Esteban, C. The Trapezium Stars. Preliminary Results on Detailed Atmosphere Modeling. In Reyes-Ruiz, M. & Vázquez-Semadeni, E. (eds.) *Revista Mexicana de Astronomía y Astrofísica Conference Series*, vol. 18 of *Revista Mexicana de Astronomía y Astrofísica*, vol. 27, 123–125 (2003).
73. Robitaille, T. P. SED Modeling of Young Massive Stars. In Beuther, H., Linz, H. & Henning, T. (eds.) *Massive Star Formation: Observations Confront Theory*, vol. 387 of *Astronomical Society of the Pacific Conference Series*, 290 (2008). 0711.4369.
74. Gaustad, J. E., McCullough, P. R., Rosing, W. & Van Buren, D. A Robotic Wide-Angle H α Survey of the Southern Sky. *PASP* **113**, 1326–1348 (2001). astro-ph/0108518.
75. Calzetti, D. *et al.* The Calibration of Mid-Infrared Star Formation Rate Indicators. *ApJ* **666**, 870–895 (2007). 0705.3377.
76. Krumholz, M. R. *et al.* Star Cluster Formation and Feedback. *Protostars and Planets VI* 243–266 (2014). 1401.2473.
77. Kruijssen, J. M. D. & Longmore, S. N. An uncertainty principle for star formation - I. Why galactic star formation relations break down below a certain spatial scale. *MNRAS* **439**, 3239–3252 (2014). 1401.4459.
78. Kennicutt, R. C., Jr., Bresolin, F., Bomans, D. J., Bothun, G. D. & Thompson, I. B. Large scale structure of the ionized gas in the magellanic clouds. *AJ* **109**, 594–604 (1995).
79. Krumholz, M. R. & McKee, C. F. A General Theory of Turbulence-regulated Star Formation, from Spirals to Ultraluminous Infrared Galaxies. *ApJ* **630**, 250–268 (2005). astro-ph/0505177.
80. Portegies Zwart, S. F., McMillan, S. L. W. & Gieles, M. Young Massive Star Clusters. *ARA&A* **48**, 431–493 (2010). 1002.1961.
81. D'Ercole, A., Vesperini, E., D'Antona, F., McMillan, S. L. W. & Recchi, S. Formation and dynamical evolution of multiple stellar generations in globular clusters. *MNRAS* **391**, 825–843 (2008). 0809.1438.

82. Bekki, K. Secondary star formation within massive star clusters: origin of multiple stellar populations in globular clusters. *MNRAS* **412**, 2241–2259 (2011). 1011.5956.
83. Schaerer, D. & Charbonnel, C. A new perspective on globular clusters, their initial mass function and their contribution to the stellar halo and the cosmic reionization. *MNRAS* **413**, 2297–2304 (2011). 1101.1073.